Batteries & Supercaps

Research Article
doi.org/10.1002/batt.202300275

Chemistry Europe
European Chemical Societies Publishing

www.batteries-supercaps.org

Carbon-Coated $NaVPO_4F$ as a High-Capacity Cathode for Aqueous Sodium-Ion Battery

Yanrong Wang,[a, b] Duan Bin,[a] Caixing Wang,[b] Yongjie Cao,[a] and Yongyao Xia*[a]

$NaVPO_4F$ has garnered significant attention as a promising cathode material for non-aqueous sodium-ion batteries due to its high theoretical specific capacity and appropriate potential. However, the dissolution of vanadium component of $NaVPO_4F$ in aqueous electrolytes has restricted its application in aqueous sodium-ion batteries (ASIBs). Herein, we report the use of carbon-coated $NaVPO_4F$ as a cathode material in ASIBs. This cathode material exhibited a discharge capacity of 111 mAh g^{-1} at 0.5 A g^{-1} in a concentrated 17 m $NaClO_4$ aqueous solution and demonstrated capacity retention of 74.4% over 100 cycles. The experimental results confirmed that the carbon coating on $NaVPO_4F$ and high-concentration $NaClO_4$ aqueous electrolyte exhibited positive effects in restraining vanadium dissolution. Additionally, when configuration with $NaTi_2(PO_4)_3$@C as anode, the full cell exhibited a capacity of 43.9 mAh g^{-1} with an average operating voltage of 1.2 V at a current density of 0.5 A g^{-1} in a concentrated 17 m $NaClO_4$ aqueous electrolyte. These outcomes underscore the potential of $NaVPO_4F$@C as a promising cathode material for ASIBs.

Introduction

Non-aqueous lithium-ion batteries show promising outlook in portable electronic devices and electric vehicles in the present stage. However, their applications face many obstacles, including rising costs rooting from the limited reserves of accessible lithium salts, and potential safety concerns from highly flammable organic electrolyte.[1–4] Nevertheless, aqueous batteries provide a safer alternative owing to the advantages of non-flammability, non-toxicity, low manufacturing cost and high ionic conductivity of electrolyte.[5–7] Especially, aqueous sodium ion batteries (ASIBs) have been considered as promising a candidate in terms of high theoretical capacity of 1160 mAh g^{-1}, low redox potential of −2.71 V vs. SHE, and the larger reserve of economically accessible sodium resources.[8–10]

Up to the present, only several cathode materials have been reported for ASIBs, including transition metal oxides (such as, $Na_{0.4}MnO_2$, $Na_{0.44}[Mn_{1-x}Ti_x]O_2$, $Na_{1.1}V_3O_{7.9}$),[11–13] Prussian blue analogues,[14,15] polyanionic compounds (such as, $Na_3V_2(PO_4)_3$, $NaVOPO_4$, $Na_4VMn(PO_4)_3$),[16–18] etc. In addition, the cathode materials usually encounter with low working potential, unsatisfying specific capacity or poor cycle stability. Recently, sodium-vanadium fluorophosphates (for instance, $NaVPO_4F$, $Na_3V_2(PO_4)_2F_3$, $Na_3V_2(PO_4)_2O_2F$, etc.) have drawn attention due to their appropriate working potentials (3.4–3.9 V *vs.* Na^+/Na) and high theoretical specific capacities (120-143 mAh g^{-1}).[19–21] Moreover, some of them have been used for sodium storage in ASIBs. The issues of electrode dissolution and inevitable hydrogen/oxygen evolution side reactions threatening their sustainability in aqueous system needs to be further resolved.[22,23]

Over the past few years, highly concentrated "water-in-salt" electrolyte (WiSE) systems have been developed to suppressed water activity, expanding the electrochemical stability window (ESW) by the formation of solid electrolyte interphase (SEI) on anode surface and absorbing hydrophobic anions on cathodes.[24–26] Recently, the WiSE systems have been used in ASIBs to improve Coulombic efficiency and cycle life of corresponding aqueous batteries.[27,28] Wang *et al.* proved that $NaCF_3SO_3$ WiSE can effectively suppress hydrogen evolution and oxygen evolution, offering an electrochemical stability window (ESW) of 2.5 V. The demostrated $Na_{0.66}[Mn_{0.66}Ti_{0.34}]O_2$/ /$NaTi_2(PO_4)_3$ ASIB exhibited excellent cycling stability over 1000 cycles.[29] Wang *et al.* reported a low-cost 19 m (m: mol kg^{-1}) $NaClO_4$-NaOTF-H_2O bi-salts WISE with a wider ESW of 2.8 V, which enables a 1.75 V $Na_3V_2(PO_4)_3$//$Na_3V_2(PO_4)_3$ ASIB, and delivers an appreciable energy density of 70 Wh kg^{-1} at 1 C with a capacity retention of 87.5% after 100 cycles.[16] Very recently, Cui et al. reported a super-concentrated aqueous electrolyte (NaTFSI in adiponitrile/H_2O), which exhibited an electrochemical stability window up to 2.75 V and the dissolution of vanadium-based electrodes and NaF-rich solidelectrolyte interphase (SEI) were greatly alleviated. The $Na_3V_2(PO_4)_3$/$NaTi_2(PO_4)_3$ full cell delivers a capacity retention of 71% after 1000 cycles at 5 C.[30]

Herein, we employed $NaVPO_4F$ with appropriate potential and high theoretical specific capacity (143 mAh g^{-1}) as cathode for ASIBs. The cycling stability of $NaVPO_4F$ was improved by two approaches, including employment of WiSE and carbon coating on the surface of $NaVPO_4F$ electrode. The carbon-coated $NaVPO_4F$ (denoted as $NaVPO_4F$@C) displays a discharge capacity of 111 mAh g^{-1} at 0.5 A g^{-1} in the first cycle, and operates over 100 cycles with capacity retention of 74.4% over 100 cycles. The

[a] Dr. Y. Wang, Dr. D. Bin, Y. Cao, Prof. Y. Xia
Department of Chemistry and Shanghai Key Laboratory of Molecular Catalysis and Innovative Materials, Institute of New Energy, iChEM (Collaborative Innovation Center of Chemistry for Energy Materials) Fudan University, Shanghai 200433, China
E-mail: yyxia@fudan.edu.cn

[b] Dr. Y. Wang, Dr. C. Wang
School of Chemistry and Chemical Engineering, Yangzhou University, Yangzhou 225002, China

Supporting information for this article is available on the WWW under https://doi.org/10.1002/batt.202300275

Research Article
doi.org/10.1002/batt.202300275
Chemistry Europe
European Chemical Societies Publishing

experimental results show that the carbon layer of $NaVPO_4F$@C and WiSE pose positive effects on restraining the vanadium dissolution of $NaVPO_4F$@C cathode in aqueous electrolyte, leading to a prolonged lifetime of $NaVPO_4F$@C cathode. In addition, the *ex-situ* XRD, *ex*-situ XPS, UV-vis spectra and ICP were adopted to investigate the energy storage and vanadium dissolving mechanism of $NaVPO_4F$@C. Then we fabricated an $NaVPO_4F$@C//$NaTi_2(PO_4)_3$@C full ASIBs in a high-concentration WiSE (17 m $NaClO_4$) aqueous electrolyte (m: mol k^{-1}). The full battery delivers a voltage of about 1.2 V and a reversible capacity of 43.9 mAh g^{-1}, calculated based on the total weight of cathode and anode electroactive materials.

Results and Discussion

$NaVPO_4F$ was synthesized via one-step soft template method. The obtained $NaVPO_4F$ was further coated with a thin carbon layer at 600 °C by chemical vapor deposition (CVD) method using toluene as the carbon source,[33] and was labelled as the $NaVPO_4F$@C. Figure 1 shows the X-ray diffraction patterns (XRD) of $NaVPO_4F$ and $NaVPO_4F$@C samples, which are in good agreement with pure monoclinic $NaVPO_4F$ (space group *C*2/*c*) reported in previous wok.[31,34] It can be seen from the XRD pattern result that the diffraction peak intensity of $NaVPO_4F$@C is slightly weaker than that of $NaVPO_4F$, due to the presence of a carbon layer on the surface of the composite. The absence of carbon in XRD patterns of $NaVPO_4F$@C composite is most likely due to the low content carbon or amorphous carbon.[33,35]

The morphology of synthesized $NaVPO_4F$@C is characterized by the scanning electron microscope (SEM) and transmission electron microscope images (TEM). As shown in Figures S1 and 2, the size of the obtained $NaVPO_4F$@C shows the morphology of nanoparticles with an average size of about several hundred nanometers. From Figure 2(a and b), it can be clearly observed that nanoparticles are coated by a thin carbon layer with about 5 nm thick. The high resolution TEM (HRTEM) image in Figure 2(c) clearly displays the crystal plane spacing of 0.2 nm, which belongs to the (131) crystal face of $NaVPO_4F$. The total elemental mappings of Na, V, P, O, F and C elements are shown in Figure 2(d–i), which illustrate a direct evidence of a uniform carbon layer distribution on the surface of $NaVPO_4F$ nanoparticles. The carbon content (~10 wt.%) of $NaVPO_4F$@C was further confirmed by thermogravimetry analysis (TGA) in Figure S2.

The electrochemical performances of $NaVPO_4F$@C cathode in traditional organic electrolyte were conducted, with 1 M $NaClO_4$ in propylene carbonate with 3 wt.% fluoroethylene carbonate as additive. As shown in Figure S3(a), the coin cell delivers an initial charge capacity and discharge capacity of 102.7 mAh g^{-1} and 97.4 mAh g^{-1} at a current density of 0.1 C, corresponding to an initial Coulombic efficiency of 94.8%. Noticeably, the average charge and discharge voltage of the cell is about 3.41 V and 3.33 V *vs.* Na^+/Na, respectively. It means that the $NaVPO_4F$@C cathode would theoretically display an appropriate potential as cathode material in (ASIBs). The cycle performance of $NaVPO_4F$@C in organic electrolyte is shown in Figure S3(b), and the cell thereafter stably operated over 300 cycles with a capacity retention of 96.2% at this low current density. In addition, the Coulombic efficiency of the coin cell gradually increased to nearly 98.6% after activation through over 25 cycles of charging and discharging process. Then, the electrochemical performance of the material in a concentrated 17 m $NaClO_4$ aqueous electrolyte was conducted extensively. Cycling voltammetry (CV) behavior of $NaVPO_4F$ and $NaVPO_4F$@C cathodes in 17 m $NaClO_4$ aqueous electrolyte was measured in a typical three-electrode system, using Ag/AgCl electrode as the reference electrode and active carbon as the counter electrode, respectively. As shown in Figure 3(a), CV of $NaVPO_4F$ shows a pair of nearly symmetric redox peaks, and the formal potential is about 0.6 V *vs.* Ag/AgCl (i.e., 0.83 V *vs.* SHE (standard hydrogen electrode)), indicating the excellent redox property of $NaVPO_4F$. The peak strength of CV curves decreased gradually in the initial 10 cycles. The charge and discharge curves of the half cell at current density of 0.5 A g^{-1} in the initial several cycles are shown in Figure 3(b), and the initial charge and discharge capacity could reach up to 101.3 and 90.9 mAh g^{-1}, respectively. The cycling performance of the $NaVPO_4F$ is shown in Figure 3(c). It is found the discharge capacity decayed rapidly to only 56 mAh g^{-1} over 100 cycles, despite the Coulombic efficiency is gradually increased from 89.8% to 99.4%. Generally, for the electrode materials in aqueous lithium or sodium-ion batteries,

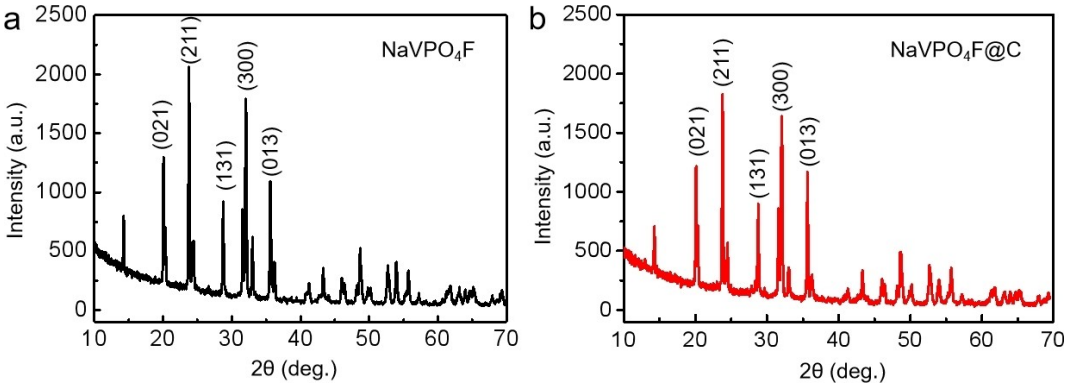

Figure 1. XRD patterns of a) $NaVPO_4F$ and b) $NaVPO_4F$@C samples, respectively.

Research Article
doi.org/10.1002/batt.202300275
Chemistry Europe
European Chemical Societies Publishing

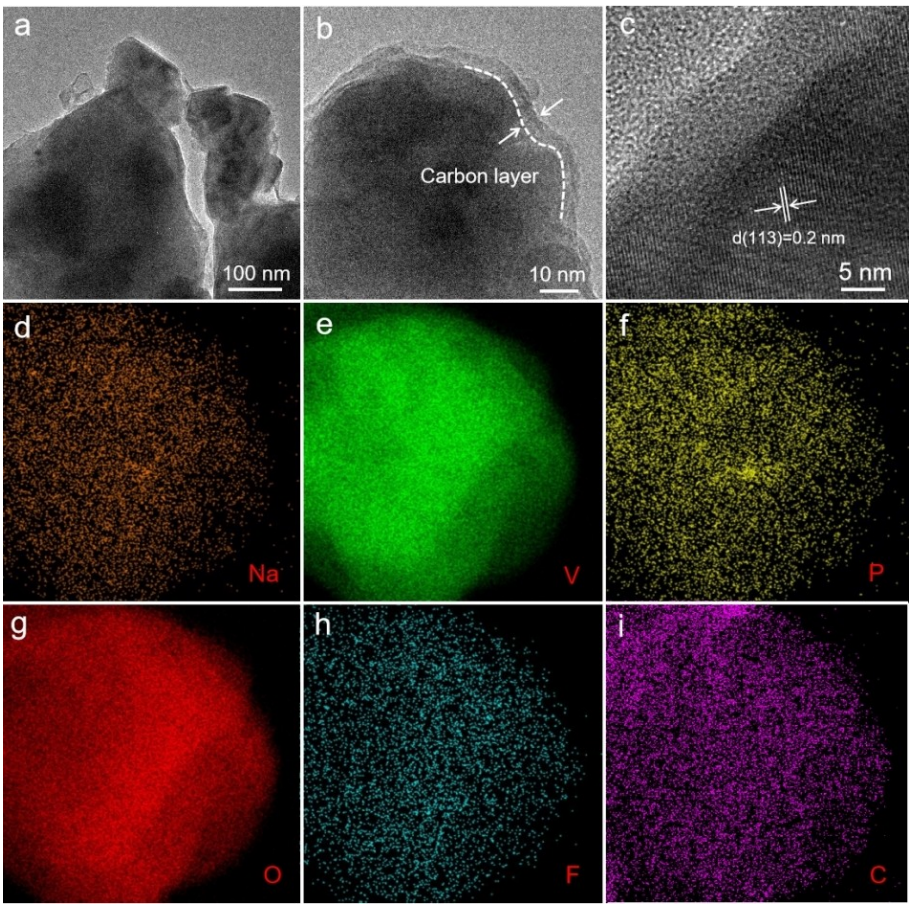

Figure 2. a, b) TEM images with different magnifications, c) HRTEM images and d–i) STEM-EDS mapping of Na, V, P, O, F and C elemental distributions on the surface of $NaVPO_4F$@C sample.

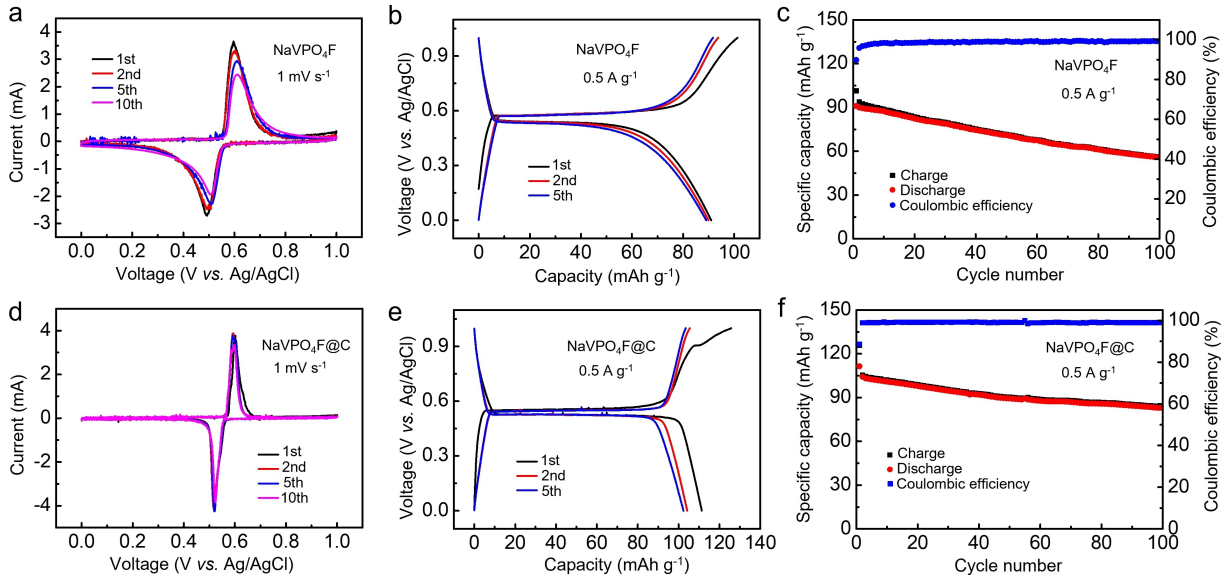

Figure 3. Electrochemical performance comparison of a–c) $NaVPO_4F$ and d–f) $NaVPO_4F$@C cathodes in aqueous 17 m $NaClO_4$. a, c) Cyclic voltammogram (CV) curves at a sweep rate of 1 mV s^{-1}. b, d) Charge-discharge curves at a current density of 0.5 A g^{-1}. c, f) Cycling performance at 0.5 A g^{-1}.

the dissolution problem could result in rapid capacity decay. Fortunately, the carbon coating on electrode could inhibit the dissolution of the materials to a certain extent.[33] Hence, the $NaVPO_4F$@C obtained by CVD method using toluene as the

Research Article
doi.org/10.1002/batt.202300275
Chemistry Europe
European Chemical Societies Publishing

carbon source was used as cathode in ASIBs. The $NaVPO_4F$@C shows a similar CV curves in aqueous electrolyte (in Figure 3d), and the peak intensity of CV curves did not decrease significantly during the initial several cycles, indicating the coated carbon layer could reduce the unwanted irreversible side reactions or dissolution of cathode in aqueous electrolyte. Figure 3(e) shows the charge and discharge curves in the initial several cycles. It can be seen that the $NaVPO_4F$@C cathode in 17 m $NaClO_4$ aqueous delivers a higher capacity, with the first charge and discharge capacities of 125.7 and 111 mAh g^{-1} at the current density of 0.5 A g^{-1}, which can be ascribed to the enhanced conductivity of carbon layer on $NaVPO_4F$@C. The cycling performance of $NaVPO_4F$@C in aqueous electrolyte is shown in Figure 3(f). The discharge capacity is 82.6 mAh g^{-1} after 100 cycles, exhibiting a much improved capacity retention of 74.4% over 100 cycles compared with $NaVPO_4F$. In order to study the impact of possible proton insertion into $NaVPO_4F$@C on the capacity fading during the discharge process, the electrochemical performances in 17 m $NaClO_4$ alkaline aqueous electrolyte with various pH values from 9 to 13 were conducted. As shown in Figure S4, $NaVPO_4F$@C shows seriously inferior electrochemical behaviors in alkaline solution with pH 13 to that in solution with pH 9 and 11. The significant oxygen evolution occurs in the alkaline solution with pH 13. Accordingly, the peak current of CV curves decreased significantly in the initial five cycles and the capacity fading is much more severe at pH 13 than that of pH 9 and PH 11. The results indicate that the capacity fading of $NaVPO_4F$@C cannot be alleviated by reducing the concentration of protons in 17 m $NaClO_4$ aqueous electrolyte. In addition, the electrochemical performance of $NaVPO_4F$@C in aqueous 0.89 m $NaClO_4$ electrolyte is also measured. As shown in Figure S5, the peak strength of CV curves obviously declines in the initial 10 cycles. The charge and discharge capacities in the first cycle were 208.7 and 102.5 mAh g^{-1}, respectively, showing a very poor Coulomb efficiency of 49.1%. The charge capacity of 208.7 mAh g^{-1} is much larger than the theoretical capacity, rooting from the vanadium dissolution of $NaVPO_4F$@C in diluted electrolyte (aqueous 0.89 m $NaClO_4$). To investigate the inhibition effect of carbon coating onto cathode and high concentration electrolyte on vanadium dissolution, electrolytes (aqueous 17 m $NaClO_4$ and 0.89 m $NaClO_4$) socked by $NaVPO_4F$@C and $NaVPO_4F$ powder for 14 days were characterized by ultraviolet-visible (UV-vis) spectrum, as shown in Figure S6(a). It can be seen that the 17 m $NaClO_4$ aqueous electrolyte socked by $NaVPO_4F$@C for 14 days exhibits the weakest UV-vis absorption spectra among the three parallel systems. This suggests that $NaVPO_4F$@C exhibits minimum vanadium chemical dissolution in concentrated 17 m $NaClO_4$. Additionally, the electrolytes cycled by $NaVPO_4F$@C and $NaVPO_4F$ were also measured by UV-vis spectrum (Figure S6b). The results show that the $NaVPO_4F$@C sample in concentrated 17 m $NaClO_4$ demonstrates the lowest vanadium dissolution during the charge-discharge process. Furthermore, the concentration of dissolved vanadium in aqueous electrolyte was tested by inductively coupled plasma (ICP), as shown in Tables S1 and S2. Both UV-vis spectra and ICP results confirmed the favorable influence of the carbon coating onto cathode and high concentration electrolyte on restraining vanadium dissolution both in chemical and electrochemical processes.

To further understand the energy storage mechanism of the cathode, *ex-situ* XRD and XPS were carried out to investigate the Na-ion storage mechanism of $NaVPO_4F$@C cathode. The *ex-situ* XRD patterns of $NaVPO_4F$@C cathode at the different charge-discharge states were collected, as shown in Figure 4(b). Most of the diffraction peaks of the pristine cathode (state *a*) can be indexed to pure monoclinic $NaVPO_4F$ except for some peaks originating from the current collector titanium mesh and binder. The peaks of (021), (211), (131) and (300) planes gradually shifted to larger angles as charging from state *a* to state *d*, which can be attributed to the decrease in crystal lattice spacing caused by Na^+-ion extraction. The peaks showed a reverse trend and shifted back to a lower angle due to the increased crystal lattice spacing caused by Na-ion insertion during the discharging process from the state *d* to state *g*, showing a reversible insertion/extraction of $NaVPO_4F$@C cathode. Figure 4(c) presents *ex-situ* V 2p X-ray photoelectron spectrometry (XPS) of the $NaVPO_4F$@C cathode at different stages, which revealed the change in the valence states of V element during the Na^+-ion extraction/insertion process. The C 1s peak (284.8 eV) is considered as the calibration in XPS spectra. The pristine electrode demonstrate two peaks at 515.8

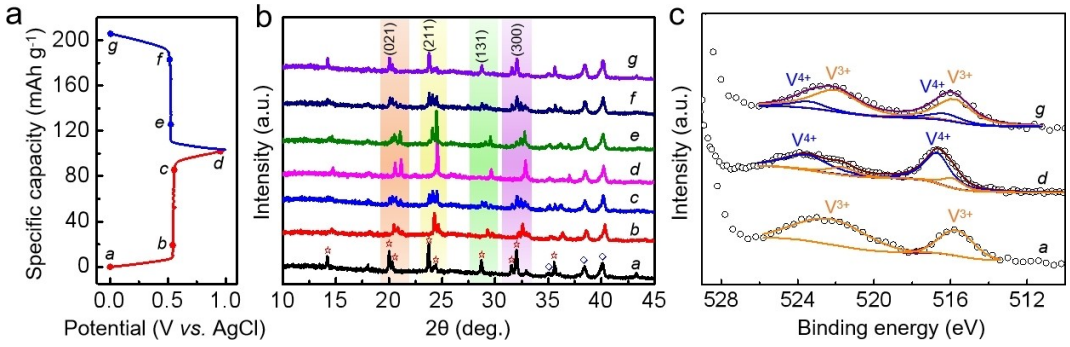

Figure 4. a) Electrochemical discharge-charge profiles of $NaVPO_4F$@C cathode at a current density of 0.5 A g^{-1}. The points labeled with *a* to *g* indicate the different discharge-charge states. b) *Ex-situ* XRD patterns (The red hollow pentacle represents pure $NaVPO_4F$, and the blue hollow diamond represents Ti mesh.) and c) V 2p XPS spectra of $NaVPO_4F$@C at pristine, oxidized and reduced states during the Na^+-ion extraction/insertion process.

Research Article
doi.org/10.1002/batt.202300275
Chemistry Europe
European Chemical Societies Publishing

and 522.5 eV, corresponding to the binding energy of V^{3+} $2p_{3/2}$ and V^{3+} $2p_{1/2}$, respectively.[20,36] When the half cell was charged completely, two new predominant peaks emerging at 516.7 and 523.5 eV can be well indexed to V^{4+} $2p_{3/2}$ and V^{4+} $2p_{1/2}$, respectively. The relative molar ratio of V^{4+} and V^{3+} is 0.78: 0.22 calculated based on the peak areas, which corresponds to the partial oxidation of V^{3+} to V^{4+} during the extraction of Na^+-ion from $NaVPO_4F$@C cathode. Subsequently, when the half cell was fully discharged, the ratio of V^{4+} to V^{3+} changed to 0.19: 0.81, which is related to the insertion of Na^+-ion into cathode. Generally, both *ex-situ* XRD and V 2p XPS spectra confirmed the charge and discharge mechanism of $NaVPO_4F$@C cathode.

Figure 5(a) shows the CV profiles of $NaVPO_4F$@C at a scan rate of 0.1 mV s^{-1}. A pair of well-defined and symmetric redox peaks appears around 0.57 V and 0.53 V *vs.* Ag/AgCl, which is consistent with charge and discharge curves of $NaVPO_4F$@C measured by three-electrode system shown in Figure 3(e). The electrode reaction kinetics of $NaVPO_4F$@C for Na^+ ion storage was then investigated by CV at various scan rates from 0.1 to 10 mV s^{-1} (Figure 5b). Theoretically, measured current obeys a power-law relationship with sweeping rates, and the voltammetric response can be summarized as the following Equation (1),[37]

$$i = av^b \quad (1)$$

where i is the current (mA), v is the sweep rate (mV s^{-1}), and a and b are adjustable parameters. The relationship between log(i) (at each peak current) and log(ν) (various scan rates) is shown in Figure 5(c). For an electrochemical process predominated by semi-infinite diffusion process, the peak current i varies with $v^{1/2}$ (i.e., $b = 0.5$), while for a capacitive-controlled reaction, i varies with v (i.e., $b = 1$). The b-value determined by the slopes of the two redox peaks are 0.43 for cathodic peaks and 0.49 for anodic peaks, respectively, implying that Na^+ storage in $NaVPO_4F$@C is dominated by the diffusion process.

Figure 6 shows the rate capability of $NaVPO_4F$ and $NaVPO_4F$@C cathodes in 17 m $NaClO_4$ aqueous electrolyte with a potential range from 0 to 1.0 V *vs.* Ag/AgCl in typical three electrode systems. The $NaVPO_4F$ cathode deliver a discharge capacity of 89.4, 82.4, 72.1, 61.7, 51.0, 37.8, 29.6 mAh g^{-1} at 0.1, 0.2, 0.5, 1, 2, 5, 10 A g^{-1}, respectively. $NaVPO_4F$ displays plateaus at about 0.56 V and 0.54 V *vs.* Ag/AgCl in charge and discharge curves, respectively. The potential gaps between charge and discharge curves become larger, and the plateaus almost disappear at 10 A g^{-1}. Apparently, $NaVPO_4F$@C cathode displays better electrochemical performance. The $NaVPO_4F$@C cathode deliver a discharge capacity of 100.7, 92.7, 88.6, 85.0, 80.5, 72.1, 62.7 mAh g^{-1} at 0.1, 0.2, 0.5, 1, 2, 5, 10 A g^{-1}, respectively. The better rate capability of $NaVPO_4F$@C than $NaVPO_4F$ is on account of the coated carbon layer, improving the electrical conductivity of $NaVPO_4F$@C cathode. The electrochemical impedance spectra (EIS) of $NaVPO_4F$@C and $NaVPO_4F$ cathodes measured in 17 m $NaClO_4$ electrolyte was further conducted, and the Nyquist plots and corresponding equivalent circuit are displayed in Figure S7. Rs is related to electrolyte and electrical contact resistance at the high-frequency region. The depressed semicircles at respective high and medium frequency regions related to charge transfer process, and the diameter of the semicircle represents the charge transfer resistance.[38] The inclined slope at low frequency region consisted of the Warburg impedance Z_w, corresponding to solid state Na^+-ion diffusion in the bulk of the electrode. The Rs value representing electrolyte and electrical contact resistance and diameter of semicircle related to charge transfer resistance for $NaVPO_4F$@C are slightly smaller than that of $NaVPO_4F$, which explains the batter rate capability of $NaVPO_4F$@C in Figure 6.

$NaTi_2(PO_4)_3$@C was selected as the anode material with a potential of appropriate 2.1 V (*vs.* Na/Na^+) flat potential plateau derived from the Ti^{4+}/Ti^{3+} redox.[33] The structure and morphology of $NaTi_2(PO_4)_3$@C sample were examined by XRD, SEM and TEM, as shown in Figures S8 and S9. The thickness of carbon layer was about 7 nm according to TEM images in Figure S9(d). The carbon content of $NaTi_2(PO_4)_3$@C was confirmed by thermogravimetry analysis (TGA) (Figure S10) to be ~20 wt.%. The electrochemical performances of $NaTi_2(PO_4)_3$@C anode in aqueous 17 m $NaClO_4$ electrolyte were investigated. Figure S11 shows the electrochemical performance in organic electrolyte (1 M $NaClO_4$ in in propylene carbonate with 3 *wt.*% fluoroethylene carbonate). Figure S11(a) shows charge-discharge profiles at 0.1 A g^{-1} in the initial three cycles. The average discharge-charge potential of $NaTi_2(PO_4)_3$@C was ~2.1 V *vs.* Na/Na^+. The discharge and charge capacities in the first cycle were 85.6 and 75.9 mAh g^{-1}, respectively, with Coulombic efficiency of 88.7%. The value of Coulombic efficiency could increase to 97.6% in the third cycle. Figure S11(b) shows the cycling

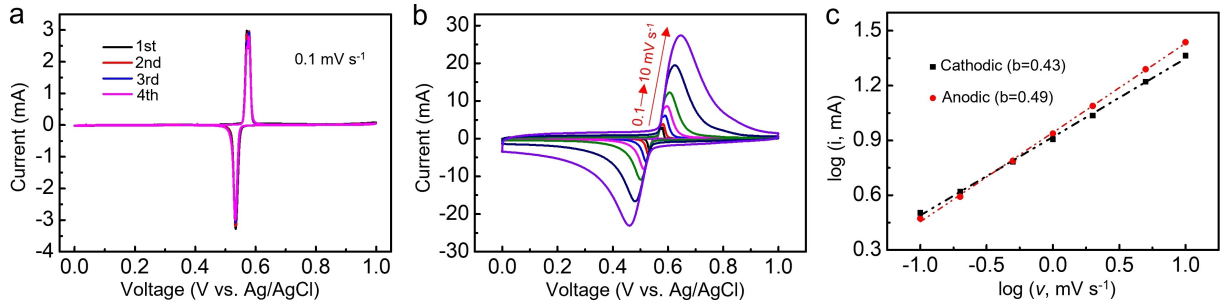

Figure 5. Kinetic analysis of $NaVPO_4F$@C for Na^+ ion storage. a) Cyclic voltammogram (CV) profiles at a sweep rate of 0.1 mV s^{-1}. b) CV curves at various scan rates from 0.1 to 10 mV s^{-1}. c) Determination of b-value according to corresponding log(i)-log(v) plots.

Research Article
doi.org/10.1002/batt.202300275
Chemistry Europe
European Chemical Societies Publishing

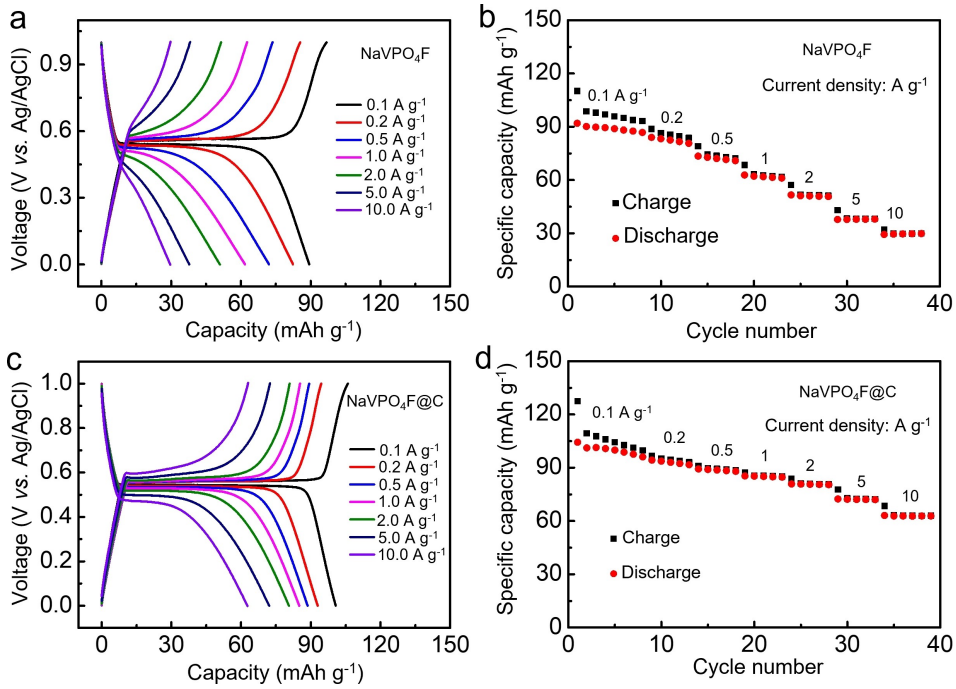

Figure 6. Rate performance of a, b) $NaVPO_4F$ and c, d) $NaVPO_4F@C$ measured at various rates from 0.1 to 10 A g^{-1} in 17 m $NaClO_4$ aqueous electrolyte, respectively.

performance of $NaTi_2(PO_4)_3@C$ at 0.1 A g^{-1} in organic electrolyte. The discharge and charge capacities increase slightly in the fifth cycle to 82.4 and 80.5 mAh g^{-1}. A stable discharge capacity of 79.7 mAh g^{-1} (96.7% of the maximum capacity) was remained after 200 cycles. The electrochemical performances of $NaTi_2(PO_4)_3@C$ in aqueous 17 m $NaClO_4$ electrolyte were further measured in a three-electrode system, as shown in Figure 7. Figure 7(a) shows CV curves of $NaTi_2(PO_4)_3@C$ at a sweeping

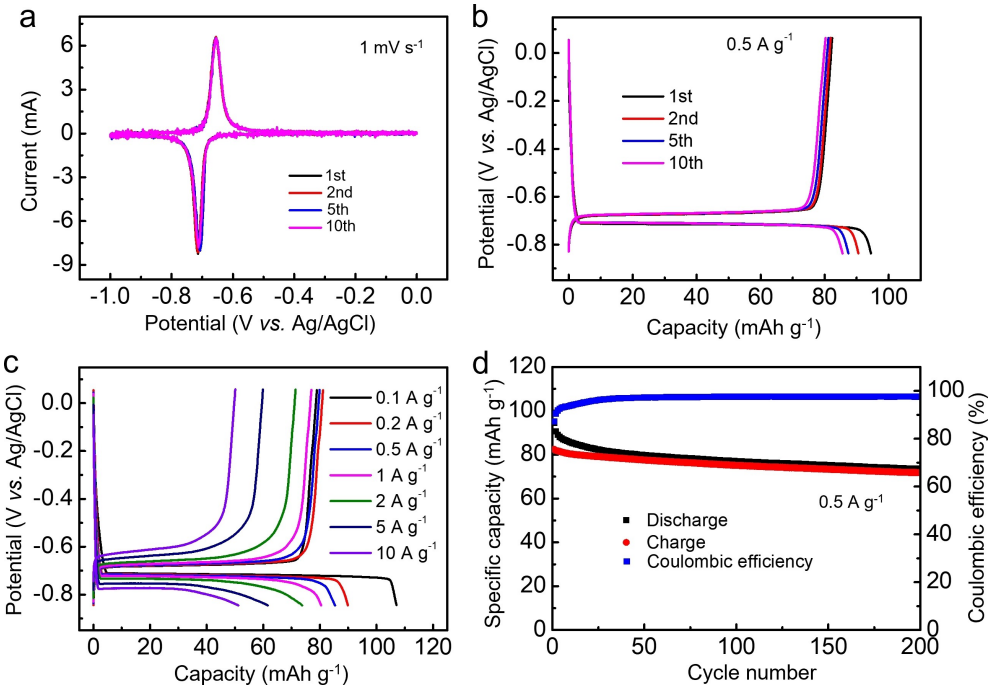

Figure 7. The electrochemical performances of $NaTi_2(PO_4)_3@C$ anode in aqueous 17 m $NaClO_4$ electrolyte in conventional three-electrode systems (Ag/AgCl as reference electrode, active carbon as counter electrode). a) CV profiles at 1 mV s^{-1} in the initial five cycles. b) Discharge-charge curves at 0.5 A g^{-1} in initial ten cycles. c) Rates capability at various current density from 0.1 to 10 A g^{-1}. (d) Cycling performance at 0.5 A g^{-1}.

Research Article
doi.org/10.1002/batt.202300275
Chemistry Europe
European Chemical Societies Publishing

rate of 1 mV s^{-1}. A pair of cathodic and anodic peaks appear at −0.713 and −0.655 V (*vs.* Ag/AgCl), corresponding to reversible Na^+-ion de-intercalation and intercalation. Besides, galvanostatic charge-discharge curves of $NaTi_2(PO_4)_3$@C at a current density of 0.5 A g^{-1} are presented in Figure 7(b), the $NaTi_2(PO_4)_3$@C anode displayed a specific discharge and capacities of 94.5 and 82.3 mAh g^{-1}, respectively, with a relatively low initial Coulombic efficiency of 87%. The Coulombic efficiency gradually increase to 93.8% in the 10th cycle. Figure 7(c) shows the rate capability at various current densities from 0.1–10 A g^{-1}. The discharge capacity was decreased from 107.1 mAh g^{-1} at the current density of 0.1 A g^{-1} to 51.2 mAh g^{-1} at the current density of 10 A g^{-1}, indicating A good rate capability of $NaTi_2(PO_4)_3$@C anode in aqueous electrolyte. Figure 7(d) depicts the cyclability of $NaTi_2(PO_4)_3$@C anode at 0.5 A g^{-1}. The discharge capacity decreases from 94.5 mAh g^{-1} in the first cycle to 73.5 mAh g^{-1} in the 200th cycle, corresponding to a capacity retention rate of ~77.8%.

The full cell was constructed with $NaVPO_4F$@C cathode and $NaTi_2(PO_4)_3$@C anode with a cathode/anode capacity ratio of 1.04:1, where the cathode is excessive to compensate the mass loss of $NaVPO_4F$@C. The calculation of the capacity for the full cell is based on the total weight of cathode and anode electroactive materials. Figure 8(a) illustrates the charge-discharge curves of the full cell at different current densities in aqueous 17 m $NaClO_4$. The full cell exhibited an average voltage plateau at ~1.26 V. The full cell delivered a specific discharge capacity of 43.9 mAh g^{-1} at a current density of 0.1 A g^{-1}. Even at a higher current density of 10 A g^{-1}, the discharge capacity could be retained at 21.7 mAh g^{-1}, indicating an excellent rate capability (Figure 8b). In Figure 8(c), a Ragone plot is depicted to show the energy density and power density of the full cell according to the charge-discharge profiles of the full cell at various current densities. A specific energy density of 54.3 Wh kg^{-1} is achieved at a power density of 66.5 W kg^{-1}. The energy density can still retain 24.9 Wh kg^{-1} at a power density of 6189.4 W kg^{-1}. Furthermore, the cycling performance of the full cell was tested at a current density of 0.5 A g^{-1}, shown in Figure 8(d). The initial specific charge and discharge capacities were 43.2 and 40.2 mAh g^{-1}, respectively, with Coulombic efficiency of 93.0%. The discharge capacities after 100 cycles gradually decreased to 19.6 mAh g^{-1}, exhibiting a capacity retention of 48.8%, with Coulombic efficiency approaching 97.6%.

Conclusions

In summary, $NaVPO_4F$@C cathode was synthesized through a one-step soft template method, followed by a chemical vapor deposition (CVD) using toluene as carbon source. The cathode exhibited a high discharge capacity of 111 mAh g^{-1} at a current density of 0.5 A g^{-1} during the initial cycle in a concentrated 17 m $NaClO_4$ aqueous electrolyte. Moreover, the cathode sustained a decent capacity retention of 74.4% after 100 cycles, demonstrating the potential for long-term cycling stability. The experimental results indicate that carbon coating on electrodes and the use of concentrated electrolyte significantly inhibit vanadium dissolution from $NaVPO_4F$ in both chemical and electrochemical processes in aqueous electrolyte. Additionally,

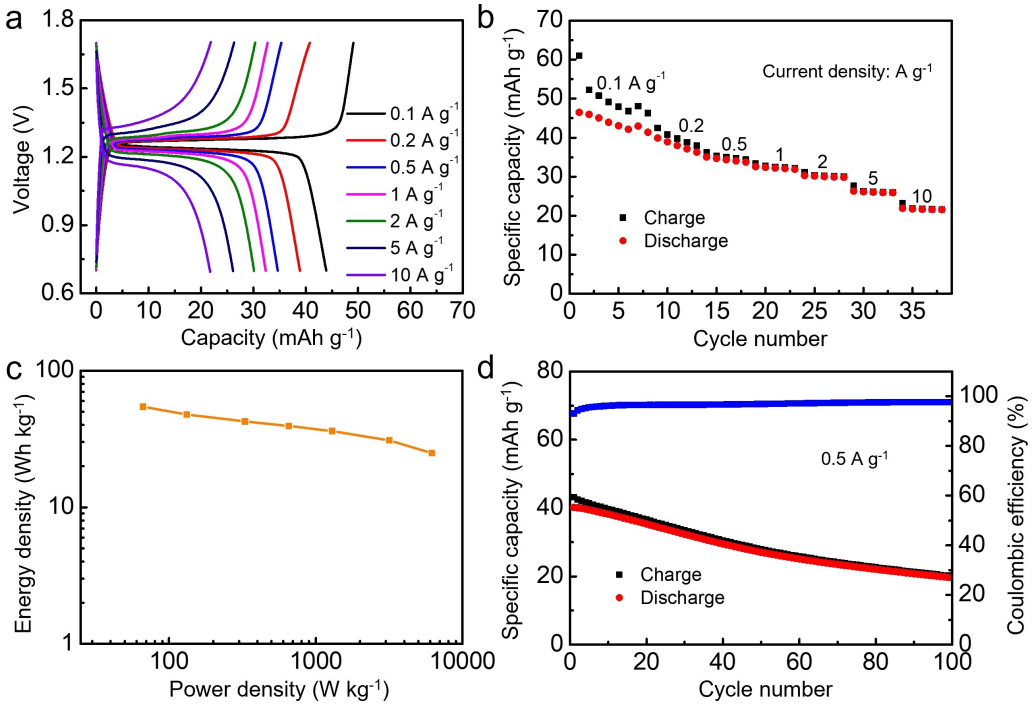

Figure 8. Electrochemical performance of the $NaVPO_4F$@C//$NaTi_2(PO_4)_3$@C full cell in aqueous 17 m $NaClO_4$. a) Galvanostatic charge-discharge curves and b) capacity stability at different current densities of at current densities range from 0.1 to 10 A g^{-1}. c) Ragone plot of the full cell. d) Capacity retention at 0.5 A g^{-1} over 100 cycles.

the carbon coating on the electrode surface also improve the electrical conductivity of $NaVPO_4F$@C. Consequently, the strategies of carbon coating and the use of concentrated electrolyte enhance the overall electrochemical performance of $NaVPO_4F$@C. Furthermore, an aqueous full cell comprising $NaVPO_4F$@C cathode and $NaTi_2(PO_4)_3$@C anode demonstrated the potential practical application of $NaVPO_4F$@C in ASIBs.

Experimental Section

$NaVPO_4F$, $NaVPO_4F$@C and $NaTi_2(PO_4)_3$@C preparation

$NaVPO_4F$ was synthesized by a modified previously reported method.[31] Typically, 1 mmol hexadecyltrimethylammonium bromide (CTAB) is added into a mixed solution containing 36 mL ethanol and 3 mL deionized H_2O. After agitating for 20 minutes, 10 mmol (0.42 g) NaF, 10 mmol (1.26 g) $C_2H_2O_4 \cdot 2H_2O$ acting as a reducing agent, 5 mmol (0.91 g) V_2O_5 in stoichiometric molar ratio were then add. After agitation for another 20 minutes, 10 mmol (1.15 g) $NH_4H_2PO_4$ is then added into the above solution. The solution was then magnetically stirring at room temperature for 24 hours, forming a homogeneous green mixture. The mixture was evaporated for several hours in the water bath at 80 °C with vigorous stirring to obtain precursor. The precursor was freeze dried for 24 hours to form green solid. The solid went through ball milling at 300 r/min for 6 hours, followed by calcining at 850 °C under argon atmosphere for 6 hours. The as-prepared $NaVPO_4F$ powder was coated with carbon layer through chemical vapor deposition (CVD) method. The as-prepared $NaVPO_4F$ powder was calcined at 600 °C for 2 hours under a N_2/toluene atmosphere and then heated up to 700 °C with toluene for another 2 hours to yield $NaVPO_4F$@C.

$NaTi_2(PO_4)_3$@C was synthesized by a sol-gel route, followed by solid-state reaction and CVD process.[32] 2 g polyvinyl ethanol (PVA) was dissolved in 100 mL H_2O under heating at 60 °C, followed by 5 mmol Na_2CO_3, 30 mmol $NH_4H_2PO_4$, 20 mmol TiO_2 were added. The mixture was evaporated in a water bath at 80 °C and a thick homogeneous gel was obtained. The gel precursor was vacuum freeze dried for 24 hours to produce the white solid. The product was then calcined at 900 °C for 12 hours at a rate of 10 °C under N_2 flow in a tube furnace, The as-prepared $NaTi_2(PO_4)_3$ powder was coated with a uniform and continuous carbon layer through CVD technology. The obtained powder was calcined at 700 °C for 4 hours under N_2/toluene atmosphere and then heated up to 900 °C with toluene for 2 hours to yield the final product $NaTi_2(PO_4)_3$@C.

Material characterization

X-ray powder diffraction (XRD) patterns of the samples were collected by a Bruker D8 X-ray diffractometer using Cu K_α ($\lambda =$ 0.15405 nm) radiation. The morphologies of the samples were characterized by S-4800 scanning electron microscope (SEM) and Joel JEM2011 transmission electron microscope (TEM). X-ray photoelectron spectroscopy (XPS) was carried on an XSAM800 Ultra spectrometer. Thermogravimetric analysis (TGA) was conducted with PerkinElmer TG209F1 instrument with O_2 flow at a ramp of 10 °C min^{-1} from 25 to 800 °C. Ultraviolet-visible (UV-vis) absorption spectra were collected by PE-Lamnda 35 UV-vis spectrometer. The concentration of dissolved vanadium in the cycled electrolyte was tested using inductively coupled plasma (ICP).

Electrochemical measurements

The working electrodes of cathode (($NaVPO_4F$ or $NaVPO_4F$@C) and anode ($NaTi_2(PO_4)_3$@C) were prepared by the mixture of active materials, conductive agent (Ketjen black), and binder (poly(tetrafluoroethylene), PTFE) in a mass of 70 : 20 : 10 in isopropanol, producing a homogeneous slurry, and then rolled into films. The films were dried in a vacuum oven at 80 °C for 10 hours prior to pressed onto titanium mesh as current collector. The electrochemical performances of $NaVPO_4F$@C cathode in traditional organic electrolyte were performed in a coin cell. A well-cut sodium metal pellet served as anode and 1 M $NaClO_4$ in propylene carbonate with 3 wt.% fluoroethylene carbonate additive served as electrolyte. The electrochemical performance of electrode materials in aqueous electrolyte systems was studied by a typical three-electrode system, where Ag/AgCl electrode ($E = 0.197$ V *vs.* SHE) and active carbon electrode served as the reference electrode and counter electrode, respectively. The optional electrolytes contain aqueous 17 m $NaClO_4$ or diluted 0.89 m $NaClO_4$ as electrolytes. In addition, the electrochemical performances of $NaVPO_4F$@C cathode were also studied in alkaline 17 m $NaClO_4$ solution with various pH values (pH 9, 11, 13), which were prepared by dissolving 17 m $NaClO_4$ in 10^{-5}, 10^{-3}, 0.1 M NaOH aqueous solution, respectively. Furthermore, the aqueous $NaVPO_4F$@C//$NaTi_2(PO_4)_3$@C cell was assembled in aqueous 17 m $NaClO_4$ solution to evaluate the overall electrochemical performance. The mass loading of working electrode was about 2.0 mg cm^{-2}. The mass ratio of $NaVPO_4F$@C cathode (~2.0 mg cm^{-2}) to $NaTi_2(PO_4)_3$@C anode (~2.35 mg cm^{-2}) is 0.85 : 1, while the capacity ratio between them is 1.04 : 1. The cyclic voltammetry (CV) measurements and electrochemical impedance spectra (EIS) with a frequency range of 100 kHz–0.1 Hz were conducted on an electrochemical workstation (CHI 660D). Galvanostatic charge-discharge and cycling stability tests were carried on Hukuto Denko battery charge-discharge system (HJ series). It should be noted that all electrochemical tests for the electrodes in aqueous electrolyte systems were carried out with vigorously bubbling N_2 to remove dissolved O_2 in electrolytes.

Acknowledgements

The authors acknowledge funding support from the National Natural Science Foundation of China (21935003, 21805126, 22209142), High-Level Entrepreneurial and Innovative Talents Program of Jiangsu, Lvyangjinfeng Talent Program of Yangzhou, and Natural Science Foundation of the Higher Education Institutions of Jiangsu Province (21KJB480006).

Conflict of Interests

The authors declare that they have no known competing financial interests or personal relationships that could have appeared to influence the work reported in this paper.

Data Availability Statement

The data that support the findings of this study are available from the corresponding author upon reasonable request.

Keywords: aqueous sodium-ion batteries · carbon coating method · concentrated $NaClO_4$ electrolyte · $NaVPO_4F$ cathode · $NaTi_2(PO_4)_3$ anode

[1] N. S. Choi, Z. Chen, S. A. Freunberger, X. Ji, Y. K. Sun, K. Amine, G. Yushin, L. F. Nazar, J. Cho, P. G. Bruce, *Angew. Chem. Int. Ed.* **2012**, *51*, 9994–10024.
[2] X. Fan, C. Wang, *Chem. Soc. Rev.* **2021**, *50*, 10486–10566.
[3] X. T. Guo, S. B. Wang, B. Yang, Y. X. Xu, Y. Liu, H. Pang, *J. Colloid Interface Sci.* **2020**, *561*, 801–807.
[4] A. K. Mondal, K. Kretschmer, Y. F. Zhao, H. Liu, C. Y. Wang, B. Sun, G. X. Wang, *Chem. Eur. J.* **2017**, *23*, 3683–3690.
[5] J. Y. Luo, W. J. Cui, P. He, Y. Y. Xia, *Nat. Chem.* **2010**, *2*, 760–765.
[6] J. Yue, J. Zhang, Y. Tong, M. Chen, L. Liu, L. Jiang, T. Lv, Y. S. Hu, H. Li, X. Huang, L. Gu, G. Feng, K. Xu, L. Suo, L. Chen, *Nat. Chem.* **2021**, *13*, 1061–1069.
[7] F. L. Zhang, W. C. Zhang, D. Wexler, Z. P. Guo, *Adv. Mater.* **2022**, *34*, 2107965.
[8] D. Bin, F. Wang, A. G. Tamirat, L. M. Suo, Y. G. Wang, C. S. Wang, Y. Y. Xia, *Adv. Energy Mater.* **2018**, *8*, 1703008–1703038.
[9] L. Jiang, L. Liu, J. Yue, Q. Zhang, A. Zhou, O. Borodin, L. Suo, H. Li, L. Chen, K. Xu, Y. S. Hu, *Adv. Mater.* **2020**, *32*, e1904427.
[10] K. J. Zhu, Z. Q. Sun, Z. P. Li, P. Liu, H. X. Li, L. F. Jiao, *Adv. Energy Mater.* **2023**, *13*, 2203708.
[11] H. Li, S. Y. Liu, T. C. Yuan, B. Wang, P. Sheng, L. Xu, G. Y. Zhao, H. T. Bai, X. Chen, Z. X. Chen, Y. L. Cao, *Acta Phys. Chim. Sin.* **2021**, *37*, 1907049.
[12] Z. Li, D. Young, K. Xiang, W. C. Carter, Y. M. Chiang, *Adv. Energy Mater.* **2013**, *3*, 290–294.
[13] Y. S. Cai, F. Liu, Z. G. Luo, G. Z. Fang, J. Zhou, A. Q. Pan, S. Q. Liang, *Energy Storage Mater.* **2018**, *13*, 168–174.
[14] C. W. Xu, Z. W. Yang, X. K. Zhang, M. T. Xia, H. H. Yan, J. Li, H. X. Yu, L. Y. Zhang, J. Shu, *Nano-Micro Lett.* **2021**, *13*, 166.
[15] J. Peng, W. Zhang, Q. N. Liu, J. Z. Wang, S. L. Chou, H. K. Liu, S. X. Dou, *Adv. Mater.* **2022**, *34*, 202108384.
[16] T. Jin, X. Ji, P. F. Wang, K. J. Zhu, J. X. Zhang, L. S. Cao, L. Chen, C. Y. Cui, T. Deng, S. F. Liu, N. Piao, Y. C. Liu, C. Shen, K. Y. Xie, L. F. Jiao, C. S. Wang, *Angew. Chem. Int. Ed.* **2021**, *60*, 11943–11948.
[17] X. Shen, M. Han, X. W. Li, P. Zhang, C. Yang, H. Z. Liu, Y. S. Hu, J. M. Zhao, *ACS Appl. Mater. Interfaces* **2022**, *14*, 6841–6851.
[18] P. R. Kumar, A. Kheireddine, U. Nisar, R. A. Shakoor, R. Essehli, R. Amin, I. Belharouak, *J. Power Sources* **2019**, *429*, 149–155.
[19] T. Jin, Y. C. Liu, Y. Li, K. Z. Cao, X. J. Wang, L. F. Jiao, *Adv. Energy Mater.* **2017**, *7*, 1700087.
[20] M. X. Ling, Q. K. Jiang, T. Y. Li, C. P. Wang, Z. Q. Lv, H. M. Zhang, Q. Zheng, X. F. Li, *Adv. Energy Mater.* **2021**, *11*, 2100627.
[21] J. Gao, Y. Tian, L. Ni, B. Wang, K. Zou, Y. Yang, Y. Wang, C. E. Banks, D. Zhang, K. Zhou, H. Liu, W. Deng, G. Zou, H. Hou, X. Ji, *Energy Environ. Mater.* **2023**, e12485.
[22] W. X. Song, X. B. Ji, Y. R. Zhu, H. J. Zhu, F. Q. Li, J. Chen, F. Lu, Y. P. Yao, C. E. Banks, *ChemElectroChem* **2014**, *1*, 871–876.
[23] S. Liu, L. B. Wang, J. Liu, M. Zhou, Q. S. Nian, Y. Z. Feng, Z. L. Tao, L. Y. Shao, *J. Mater. Chem. A* **2019**, *7*, 248–256.
[24] L. M. Suo, O. Borodin, T. Gao, M. Olguin, J. Ho, X. L. Fan, C. Luo, C. S. Wang, K. Xu, *Science* **2015**, *350*, 938–943.
[25] D. W. Xiao, L. Zhang, Z. W. Li, H. Dou, X. G. Zhang, *Energy Storage Mater.* **2022**, *44*, 10–28.
[26] J. Han, A. Mariani, S. Passerini, A. Varzi, *Energy Environ. Sci.* **2023**, *16*, 1480–1501.
[27] M. Kumar, T. C. Nagaiah, *Energy Storage Mater.* **2022**, *49*, 390–400.
[28] A. Yamada, A. Kitada, S. Ko, R. Ikeya, Y. Yamada, *J. Phys. Chem. C* **2023**, *127*, 3432–3436.
[29] L. M. Suo, O. Borodin, Y. S. Wang, X. H. Rong, W. Sun, X. L. Fan, S. Y. Xu, M. A. Schroeder, A. V. Cresce, F. Wang, C. Y. Yang, Y. S. Hu, K. Xu, C. S. Wang, *Adv. Energy Mater.* **2017**, *7*, 1701189–1701198.
[30] H. Wang, T. T. Liu, X. F. Du, J. Z. Wang, Y. Y. Yang, H. Y. Qiu, G. L. Lu, H. L. Li, Z. Chen, J. W. Zhao, G. L. Cui, *Batteries & Supercaps* **2022**, *5*, e202200246.
[31] M. Law, P. Balaya, *Energy Storage Mater.* **2018**, *10*, 102–113.
[32] L. Chen, J. Y. Liu, Z. W. Guo, Y. G. Wang, C. X. Wang, Y. Y. Xia, *J. Electrochem. Soc.* **2016**, *163*, A904-A910.
[33] G. N. Zhu, C. X. Wang, Y. Y. Xia, *J. Electrochem. Soc.* **2011**, *158*, A102-A109.
[34] M. X. Ling, F. Li, H. M. Yi, X. F. Li, G. J. Hou, Q. Zheng, H. M. Zhang, *J. Mater. Chem. A* **2018**, *6*, 24201–24209.
[35] D. Bin, Y. R. Wang, A. G. Tamirat, P. Zhu, B. B. Yang, J. Wang, J. H. Huang, Y. Y. Xia, *ACS Sustain. Chem. Eng.* **2021**, *9*, 3223–3231.
[36] C. C. Chen, T. J. Li, H. Tian, Y. B. Zou, J. C. Sun, *J. Mater. Chem. A* **2019**, *7*, 18451–18457.
[37] P. Simon, Y. Gogotsi, B. Dunn, *Science* **2014**, *343*, 1210–1211.
[38] D. Aurbach, *J. Power Sources* **2000**, *89*, 206–218.

Manuscript received: June 29, 2023
Revised manuscript received: July 26, 2023
Version of record online: August 4, 2023